APPLIED PHYSICS

Integrated quantitative PIXE analysis and EDX spectroscopy using a laser-driven particle source

F. Mirani[1]*, A. Maffini[1], F. Casamichiela[1], A. Pazzaglia[1], A. Formenti[1], D. Dellasega[1], V. Russo[1], D. Vavassori[1], D. Bortot[1], M. Huault[2,3], G. Zeraouli[2,3], V. Ospina[2,3†], S. Malko[2,3], J. I. Apiñaniz[2], J. A. Pérez-Hernández[2], D. De Luis[2], G. Gatti[2], L. Volpe[2,4], A. Pola[1], M. Passoni[1]*

Among the existing elemental characterization techniques, particle-induced x-ray emission (PIXE) and energy-dispersive x-ray (EDX) spectroscopy are two of the most widely used in different scientific and technological fields. Here, we present the first quantitative laser-driven PIXE and laser-driven EDX experimental investigation performed at the Centro de Láseres Pulsados in Salamanca. Thanks to their potential for compactness and portability, laser-driven particle sources are very appealing for materials science applications, especially for materials analysis techniques. We demonstrate the possibility to exploit the x-ray signal produced by the co-irradiation with both electrons and protons to identify the elements in the sample. We show that, using the proton beam only, we can successfully obtain quantitative information about the sample structure through laser-driven PIXE analysis. These results pave the way toward the development of a compact and multifunctional apparatus for the elemental analysis of materials based on a laser-driven particle source.

INTRODUCTION

Analytical techniques of x-ray emission spectroscopy play a crucial role in many fields of materials science. They rely on the irradiation of samples with ionizing radiation and the detection of the emitted characteristic x-rays. The elements are recognized according to the x-ray energies, while their concentrations are retrieved from the number of counts. The analytical capabilities of a specific technique depend on the type of incident particles. For instance, a very common technique is the x-ray fluorescence (XRF) spectroscopy (1), which exploits an x-ray source to induce secondary emission of characteristic x-rays. XRF is a method for the multielemental analysis of homogeneous samples. Another widespread technique able to quickly provide the elemental composition of solid samples is the energy-dispersive x-ray (EDX) (2) spectroscopy. Conventional EDX is performed only in vacuum, and the probed thickness is of micrometers. Another powerful nondestructive technique is particle-induced x-ray emission (PIXE) (1, 3). Exploiting MeV energy protons, PIXE provides both elemental concentrations of homogeneous samples and stratigraphic structures of complex artifacts down to a few tens of micrometers. Unlike EDX, PIXE can also be performed in air. Since its birth, the extensive use of PIXE has been limited by the use of large accelerators. Both EDX and PIXE are widely exploited in semiconductor industry (4, 5), environment monitoring (6, 7), and cultural heritage preservation (8, 9). These fields could substantially benefit from the adoption of a flexible, multiparticle tool for x-ray emission spectroscopy with different capabilities.

Laser-driven sources (10, 11) are worth of consideration for materials science applications (12–15). A common acceleration scheme exploits the interaction between ultrashort (tens of fs) super-intense ($I > 10^{18}$ W/cm^2) laser pulses and micrometric solid targets to accel-

erate electrons and protons to energies ranging from few MeV up to hundreds of MeV. Electrons and protons are accelerated together in an ultrafast dynamics, and their energy spectra are broad. Because of their peculiar features, compact [e.g., a few meters size (16–19)] laser-driven accelerators could be exploited for EDX (20) and PIXE (21–23). A proof-of-principle elemental PIXE analysis of a homogeneous sample (i.e., the identification of the elements present in the sample) exploiting a laser-driven particle source was demonstrated by Barberio et al. (22). Since the range of MeV energy electrons in solids is of several millimeters, they could be used to detect elements deeper inside samples compared to keV electrons. Moreover, MeV electrons can propagate for hundreds of centimeters in air, thus enabling ex situ EDX on large surfaces. Furthermore, the current laser technology provides table-top tens of TW class lasers (24), which can accelerate protons up to the energies required by PIXE.

In this work, we experimentally perform elemental analysis of a nonhomogeneous sample exploiting a laser-driven source. To that end, we present the first elemental laser-driven EDX (LD-EDX) and the first quantitative laser-driven PIXE (LD-PIXE) analysis. The experiment was performed at the Centro de Láseres Pulsados with the Vega-2 laser (25).

We propose two setups to exploit at best the laser-driven charged-particle source, performing the sample irradiation either with both electrons and protons (Fig. 1A) or only with protons (Fig. 1B). We show that the x-ray yield induced by electron irradiation is dominant in the first configuration (hence, we call it LD-EDX setup) and it can be exploited to effectively identify the elements. Under the second irradiation condition (LD-PIXE setup), we practically demonstrate that an LD-PIXE signal can be used to retrieve quantitative stratigraphic information about the sample structure. We support our experimental results through a Monte Carlo investigation of both setups.

RESULTS AND DISCUSSION

LD-EDX and LD-PIXE experimental setups

In both LD-PIXE and LD-EDX setups, the 200-TW Vega-2 laser pulse interacts with a micrometric aluminum foil to accelerate electrons and protons toward the sample placed in the vacuum chamber. We interpose a second aluminum sheet between the laser-driven particle

[1]Politecnico di Milano, Via Ponzio 34/3, I-20133 Milan, Italy. [2]Centro de Laseres Pulsados (CLPU), Edicio M5. Parque Científico. C/ Adaja. 8. Villamayor, 37185 Salamanca, Spain. [3]Universidad de Salamanca, Patio de Escuelas 1, 37008 Salamanca, Spain. [4]Laser-Plasma Chair at the University of Salamanca, Salamanca, Spain.
*Corresponding author. Email: francesco.mirani@polimi.it (F.M.); matteo.passoni@polimi.it (M.P.)
†Present address: Université de Bordeaux, CNRS, CEA-DAM/DIF, CELIA (Centre Lasers Intenses et Applications), UMR 5107, Talence, France.
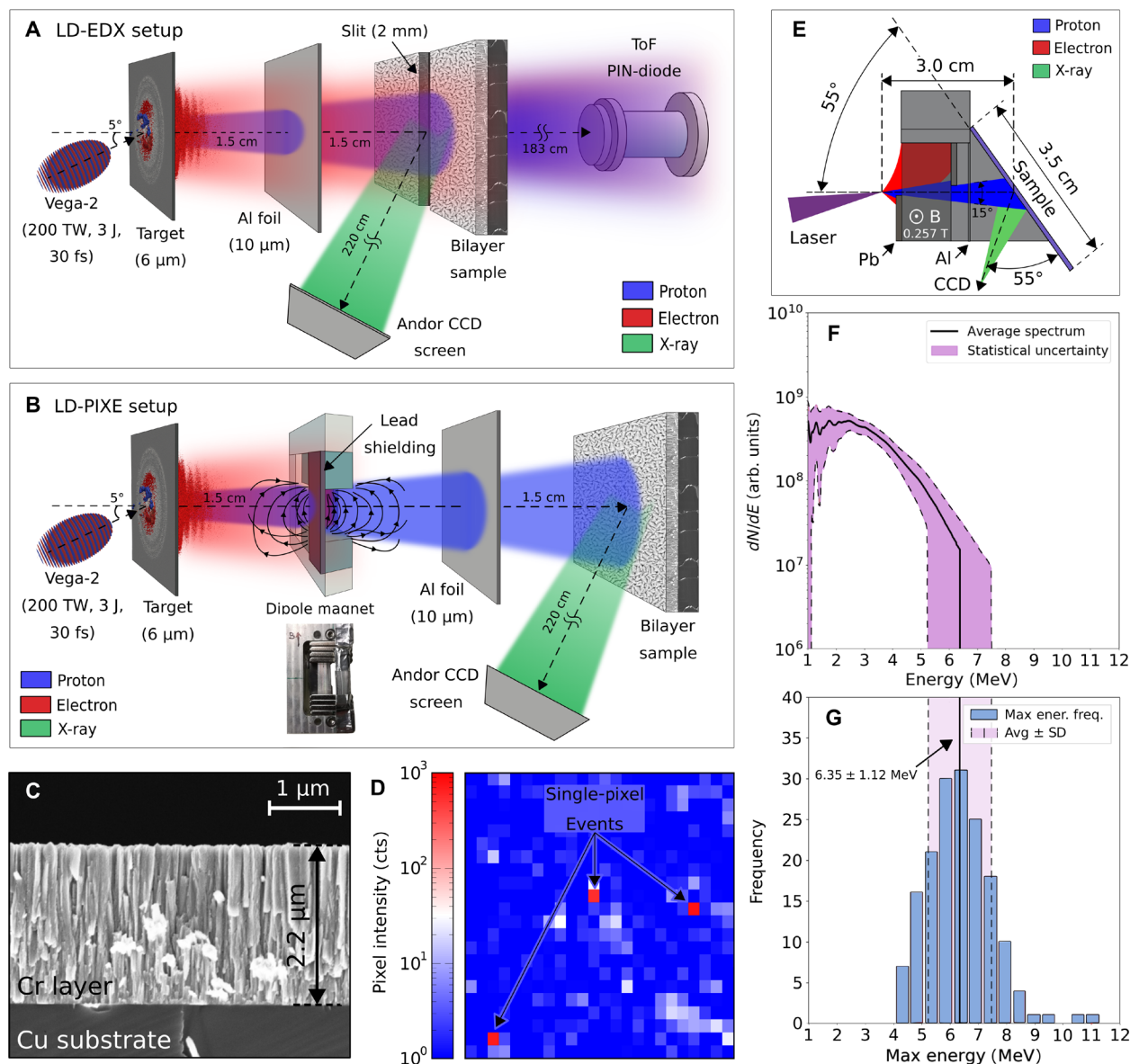
Fig. 1. Conceptual schemes of the experimental setups. (**A**) Schematic illustration for the LD-EDX setup. (**B**) Schematic illustration for the LD-PIXE setup. (**C**) Scanning electron microscope (SEM) cross-sectional view of the irradiated sample. (**D**) Detail of a recorded charge-coupled device (CCD) image for x-ray detection. Single-pixel events are indicated. (**E**) Top view scheme of the LD-PIXE setup. (**F**) Proton energy spectrum recorded with time-of-flight (ToF) spectrometer. No absolute calibration is provided on the vertical axis. The continuous black line is the average spectrum. The purple area represents the statistical uncertainty (i.e., ±SD), provided as the superposition of two separated contributions: the uncertainty on the signal for any energy value and the uncertainty on the maximum proton energy. (**G**) Absolute frequency distribution for the maximum proton energy recorded with ToF measurements. The vertical line represents the mean value, while the purple band width is two times the SD. Photo credit: Francesco Mirani, Politecnico di Milano.

source and the sample to stop the debris produced by the laser-target interaction. The sample has the same composition in both setups. It is made of a 2.2-μm-thick layer of chromium deposited onto a 1-mm-thick substrate of pure copper. Oxygen is present as a contaminant (<10%) in the Cr layer. The film density is equal to 5.3 g/cm^3. A cross-sectional view of the sample is shown in Fig. 1C. Details about the sample production are provided in Materials and Methods. To detect the emitted x-rays, we exploit a charge-coupled device (CCD). The experimental setups are designed to allow a postprocessing, single-photon counting spectra reconstruction (*26, 27*). Single-photon

events can be clearly distinguished in Fig. 1D. The CCD energy calibration (see Materials and Methods) was done through the irradiation of a pure Cu sample with the LD-EDX setup.

Since the LD-EDX setup has the dual purpose of irradiating the sample and characterizing the accelerated protons, we created an aperture slit in the middle of the sample so that a fraction of the protons could reach the ion diagnostics. In the LD-PIXE setup, the sample is not split and a 0.26-T dipole magnet and lead shields are placed behind the target to remove the electrons (see Fig. 1E). Further details about the setups are provided in Materials and Methods.

The proton diagnostics in the LD-EDX setup is a time-of-flight (ToF) spectrometer (see Materials and Methods) (28, 29), which is aligned with the sample slit along the target normal direction. The energy spectrum averaged over 166 shots, as well as the statistical uncertainty, is shown in Fig. 1F. In Fig. 1G, we report the absolute frequency distribution of maximum proton energy (average value, 6.35 MeV; SD, 1.12 MeV). It is worth mentioning that the knowledge of the shape and the cutoff energy of the proton spectrum is fundamental for LD-PIXE analysis as shown below.

LD-EDX elemental and LD-PIXE stratigraphic analyses

We start by discussing the LD-EDX spectrum. The goal is to perform elemental analysis, i.e., the identification of the elements present in the sample. Then, we focus on the quantitative characterization of the sample structure through LD-PIXE analysis. This method allows us to retrieve further information about the composition [e.g., the elemental concentrations in homogeneous samples (21)] starting from the x-ray line intensities. For the present study, since the layer and substrate are monoelemental, the method is applied to determine the Cr layer thickness. Therefore, for the specific case considered here, we call this procedure stratigraphic analysis.

We irradiate the sample with 42 particle bunches (i.e., shots) in the LD-EDX setup. The corresponding x-ray spectrum per unit of shots is presented in Fig. 2A. As expected, well-defined peaks emerge from the background. The fit is performed with the Levenberg-Marquardt least-square fitting algorithm (30), a standard method for x-ray spectra interpolation. The peaks are fitted with a Gaussian shape (31), while the background is modeled with an exponential polynomial of third order (31). Figure 2A also shows the fitted Cr and Cu peaks after background subtraction. Unlike Cu, in the case of Cr, the Kβ line cannot be distinguished. This is due to a partial superposition with the Kα peak and the presence of an intense background signal. For the present study, the intent is to identify both Cr and Cu elements (the detection efficiency of the shielded CCD is too low at the energy corresponding to the oxygen line). Figure 2B lists the energies of the x-ray peaks. They are very close to the actual values, with a relative deviation always less than 2%. Since we can uniquely identify the elements, we can conclude that LD-EDX provides a reliable elemental analysis.

Unlike the elemental analysis, the stratigraphic analysis requires a model that relates the x-ray yields, the material composition, and the energy of the incident particles. As far as LD-EDX is concerned, the electron spectrum characterization is not trivial. Moreover, no analytical models to describe the x-ray emission induced by high-energy electrons are available. Therefore, the x-ray spectrum obtained by LD-EDX cannot be directly interpreted to retrieve stratigraphic information. To obtain the latter, both reference samples and prior knowledge of the accelerated electron spectrum would be needed (32).

To overcome the aforementioned limitations, we switch to LD-PIXE. The LD-PIXE spectrum (Fig. 2C) is obtained with 16 particle bunches. In addition, in this case, several peaks are visible. Besides the Cr and Cu characteristic peaks, the spectrum also shows the Pb-Kα signal due to the lead shields. In addition, we can recognize a weak signal at 6.3 keV, likely to be related to the iron in the magnet. As for LD-EDX, all elements are correctly recognized as well. However, the x-ray signal per shot obtained with the LD-PIXE setup is approximately 10 times less intense than that recorded using the LD-EDX setup coherently with published theoretical results (20).

Therefore, we conclude that LD-EDX provides the sample elemental analysis with a lower number of shots compared to LD-PIXE.

On the other hand, the x-ray yields obtained with the LD-PIXE setup can be exploited for stratigraphic analysis. We have proposed an analytical model and a procedure to determine the sample structure from an LD-PIXE measurement (21). For the specific case considered here, the mass thickness of the Cr layer can be evaluated by solving Eq. 5 presented in Materials and Methods. It relates the x-ray intensity ratio (i.e., Cr/Cu reported in Fig. 2B), the film composition, and the incident proton spectrum shape. The x-ray yields (i.e., intensities) are evaluated as the area subtended by the Gaussian peaks after background subtraction. Figure 2D shows the comparison between the sample cross section and the reconstructed thickness from LD-PIXE analysis. Assuming a pure Cr film and Cu substrate, i.e., neglecting the presence of oxygen, we estimate a layer thickness of 1.90 ± 0.39 μm using the ratio of Cr and Cu x-ray yields obtained experimentally. Considering also the presence of 7% oxygen in the Cr film, we find a thickness equal to 2.01 ± 0.39 μm, which is even closer to the actual value of 2.2 μm. We evaluated the error through a Monte Carlo approach (33), taking into account the uncertainty of both x-ray and proton spectra (see Materials and Methods). They contribute almost equally to the overall uncertainty, which can therefore be reduced by increasing the number of shots, optimizing the detection system, or improving the proton source reproducibility. The last point can be achieved by optimizing the target manufacturing and the laser stability. Another small source of uncertainty is represented by a partial overlap of the Kα and Kβ lines of Cr. This can be avoided by exploiting a detector with higher energy resolution. Last, few electrons still interact with the sample with the LD-EDX setup. Therefore, they can slightly contribute to the spectrum in Fig. 2C, and they can affect the thickness measurement. This last point will be extensively addressed in the following section. Anyhow, even under the present experimental conditions, LD-PIXE provides a satisfactory estimation of the actual thickness. Last, Fig. 2D also reports the thickness evaluated considering the yield ratio obtained with the LD-EDX setup (i.e., assuming to ignore the presence of the incident electrons in the LD-PIXE measurement). The result of 0.98 ± 0.16 μm strongly underestimates the actual chromium thickness. Since electrons are more penetrating compared to protons, they unbalance the yield ratio in favor of the copper.

In light of the obtained results, we can conclude that (i) because of the high intensity of the x-ray signal, the recommended setup to perform elements identification is the LD-EDX one. (ii) On the other hand, the quantitative stratigraphic analysis requires removing the electron contribution to the x-ray signal. Therefore, LD-PIXE must be exploited. (iii) The knowledge of the absolute number of incident protons is not required to perform LD-PIXE analysis. This is very convenient from the experimental point of view since no absolute calibration of the proton detector is needed. (iv) With a suitable theoretical description of LD-PIXE (21), the monochromaticity of the incident proton spectrum is not required.

We can also draw further fundamental prospects regarding the potential of the approach that we are presenting: (i) The large range of MeV electrons in solids can open to the possibility of the analysis down to hundreds of micrometers depth. At these energies, the electron impact ionization cross sections (34) for the Kα shells of heavy elements become substantial. Moreover, the associated x-ray energies are of the order of tens of keV and are thus subject to weak attenuation in thick layers. These considerations suggest that LD-EDX should
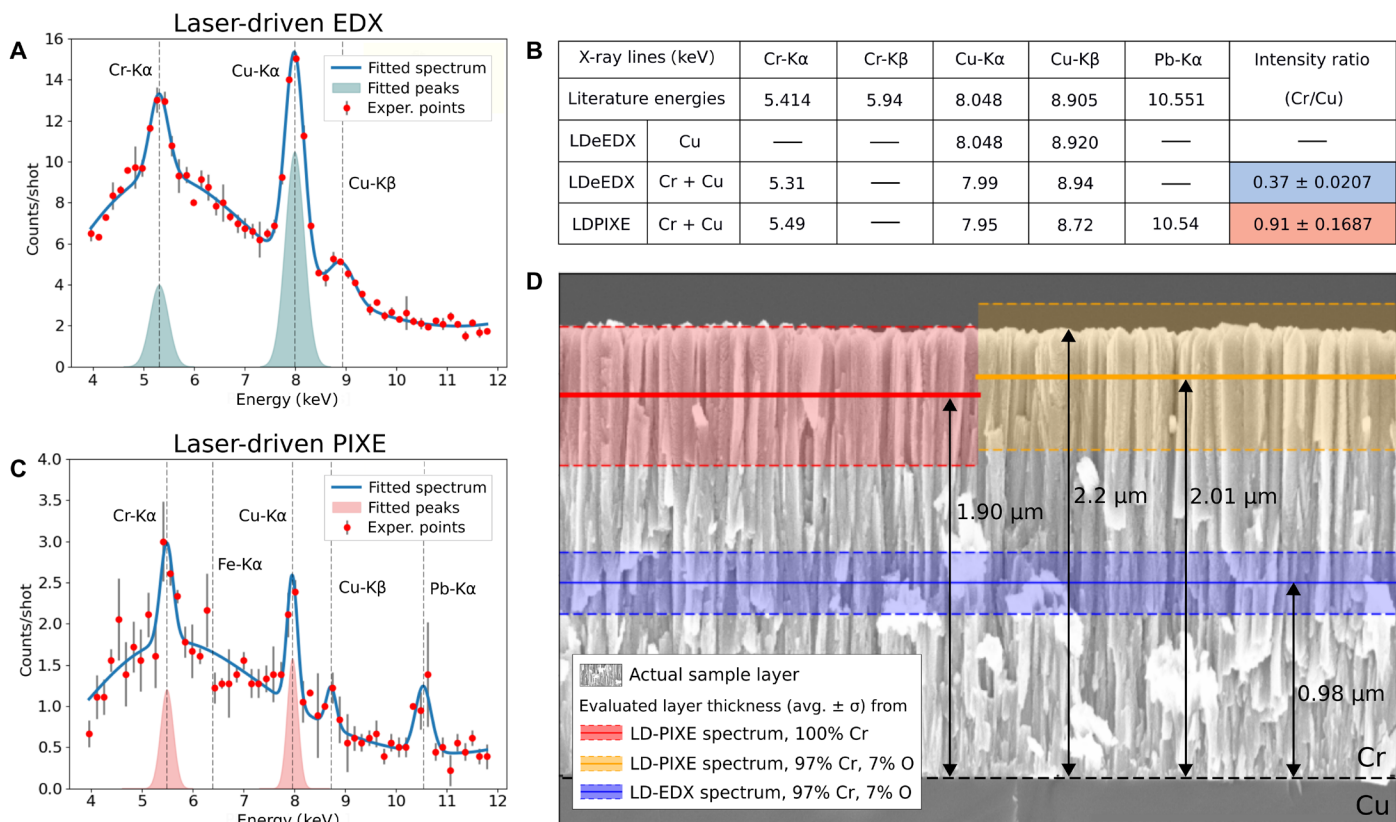
Fig. 2. Laser-driven electron EDX/PIXE results. (**A**) Recorded spectrum with the LD-EDX setup. The red points are the average over the shots of x-ray intensity at each photon energy, while the length of the error bars is two times the SD. The blue line is the fitted spectrum. The filled blue curves are the Gaussian fits for the peaks. (**B**) Summary of the recorded x-ray line positions and intensity ratios of the Cr and Cu peaks. The first row reports the expected x-ray energies from literature. The second row is related to the x-ray spectrum used to calibrate the CCD (see Materials and Methods), while the last two rows list the peak positions in the spectra, expressed as the centroid of the fitting Gaussian. (**C**) Recorded spectrum with the LD-PIXE setup. The filled red curves are the Gaussian fits for the peaks. (**D**) Results of the LD-PIXE stratigraphic analysis. The red and yellow lines are retrieved from the yield ratio obtained from the LD-PIXE measurement. The red line is the thickness retrieved assuming a 100% Cr film. The yellow line is the thickness obtained assuming a 93% Cr and 7% O film. The blue line is the thickness obtained assuming the yield ratio from the LD-EDX measurement and a 93% Cr and 7% O film. The color-filled regions represent the statistical uncertainties.

allow us to recognize the presence of heavy elements in matrices within the millimeter thickness range, significantly extending the capabilities of EDX. (ii) Note that the results here presented for a 200-TW laser should be obtained exploiting compact tens of TW class lasers (*35, 36*). They can provide protons with maximum energy of ~6 MeV. Moreover, compact lasers operate with a repetition rate equal to 10 Hz. Assuming a number of accelerated protons of 10^9 to 10^{10} particles per shot and the aforementioned repetition rate, the resulting current is approximately 1 to 10 nA. These values are compatible with the currents exploited in conventional PIXE analysis for cultural heritage studies (*37*). (iii) Laser-driven ion sources offer several solutions to quickly modify the shape of the spectrum of the accelerated particles. The maximum energy of the accelerated protons can be reduced by decreasing the laser power (*38*). The same result can be achieved by also fixing the laser power and exploiting targets with larger thicknesses (*36*). Moreover, the proton maximum energy can be increased using advanced target configurations (e.g., near-critical double-layer targets) (*39–41*). The possibility to easily tune the maximum energy of the accelerated protons could be exploited to perform the analysis of complex nonhomogeneous structure by means of differential PIXE.

Assessment of the electron influence on LD-PIXE via Monte Carlo simulations

In light of the results presented in the previous section, a proper characterization of the system exploited to remove the electrons in the LD-PIXE setup is necessary. The thickness obtained from LD-PIXE analysis (i.e., 2.01 μm) underestimates the actual thickness (i.e., 2.2 μm) of about 10%. We can suppose that, even in the presence of the magnet in the LD-PIXE setup, a residual fraction of electrons can reach the sample. Therefore, the fraction of x-rays due to the electrons irradiation compared to the amount induced by protons must be properly estimated. Thus, we performed Geant4 (*42*) Monte Carlo simulations of the charged-particles propagation, their interaction with the sample, and x-ray generation.

We simulate LD-EDX and LD-PIXE analysis considering both protons and electrons as primary particles. The simulated setups are shown in Fig. 3 (A and B). Simulations are performed with the same number (10^8) of electrons N_e and protons. The primary particles are generated with a uniform angular distribution between ±20° so that the sample surface is entirely hit by the particles. The proton energies are extracted from the measured energy distribution (Fig. 1F). On the other hand, the electron energy spectrum is modeled as an
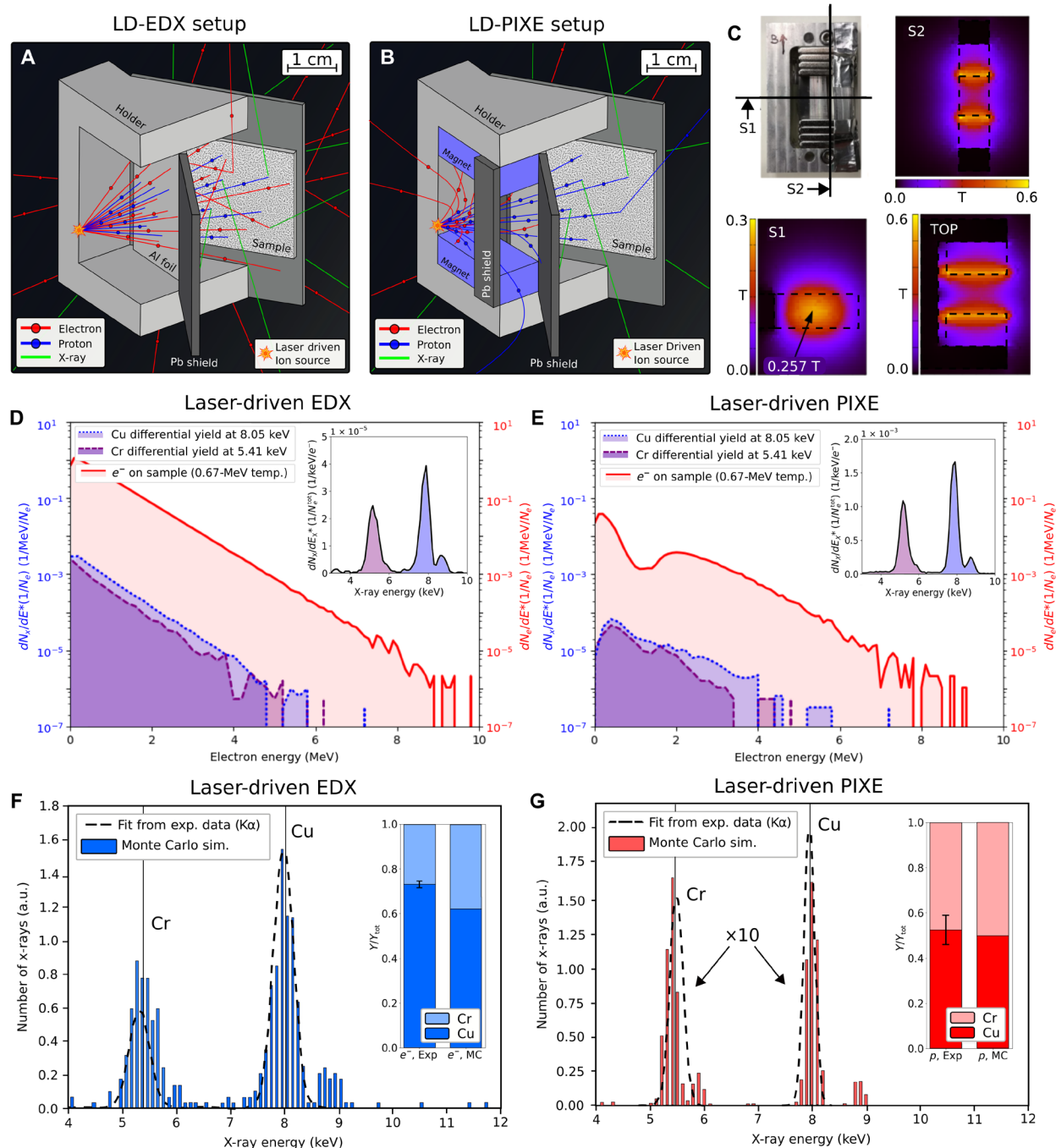
Fig. 3. Finite element method (FEM) and Monte Carlo simulations of LD-EDX/PIXE. (**A** and **B**) Snapshots of the LD-EDX and LD-PIXE Monte Carlo simulations. (**C**) Slices of the magnetic field intensity distribution in the LD-PIXE setup obtained with FEM analysis. In the first panel, the position of the S1 and S2 slices is marked, while the TOP slice is taken parallel to the top view and passes through the center of the magnet. (**D** and **E**) LD-EDX and LD-PIXE Monte Carlo simulation outputs for electrons with initial temperature of 0.67 MeV as primary particles. The filled red areas are the energy spectra of the electrons incident on the sample surface. The filled blue curves are the x-ray differential yields. The inset graphs are the simulated x-ray spectra associated with electrons in LD-EDX and LD-PIXE setups, respectively. (**F** and **G**) Comparison between the simulated peaks and fits from experimental data for LD-EDX and LD-PIXE. The inset graphs compare the experimental and simulated x-ray yield ratios for LD-EDX and LD-PIXE. a.u., arbitrary units. Photo credit: Francesco Mirani, Politecnico di Milano.

exponential distribution with maximum energy of 10 MeV. We considered two electron temperatures equal to 0.67 and 1.0 MeV. The first value is estimated from the actual laser parameters using a generalized ponderomotive scaling (*43*). The second temperature is ob-

tained by matching the theoretical estimation of the maximum proton energy [provided by the Passoni-Lontano model (*44*)] and the corresponding experimental value. For a detailed description of the equations for the temperature evaluations, please refer to Materials

and Methods. To properly simulate the LD-PIXE setup, we first evaluate the three-dimensional (3D) magnetic field intensity distribution by means of a magnetostatic finite element analysis (mFEA) (45). The resulting intensity map is shown in Fig. 3C. Then, we include the 3D magnetic field distribution in the Geant4 simulation. The mFEA simulation is extensively described in Materials and Methods, and a full presentation of the Monte Carlo code implementation is provided in already published works (20, 21).

We start considering the simulations with electrons as primary particles. For the 0.67-MeV electron temperature, the simulated energy spectra for the LD-EDX and LD-PIXE setups are shown in Fig. 3 (D and E, respectively). All data are normalized to the total number of simulated primary electrons. Since in the LD-EDX setup particles are not deflected, the spectrum of the electrons impinging on the sample practically coincides with the input exponential one. On the other hand, in the LD-PIXE setup, the number of electrons reaching the sample surface is drastically lowered because of the effect of the magnet. Overall, about 98% of the incident electrons are removed in the case of 0.67-MeV temperature. With a temperature of 1.0 MeV, 96.3% of the incident electrons are removed. Figure 3 (D and E) also shows the x-ray differential yields. They are defined as the number of characteristic x-rays (i.e., at 5.41 and 8.05 keV for Cr and Cu, respectively), leaving the sample as a function of the incident electron energy. The differential yields confirm that MeV electrons contribute to the x-ray production because the substrate is thick enough to let them slow down. The ratios between the x-ray yields due to the electrons in the presence and absence of the magnet (i.e., $Y_{LD-PIXE, e}/Y_{LD-EDX, e}$) are 0.020 and 0.036 for the 0.67- and 1.0-MeV electron temperatures, respectively. On the other hand, the experimental ratio between the x-ray yields in LD-EDX and LD-PIXE $[(Y_{LD-EDX, e} + Y_{LD-EDX, p})/(Y_{LD-PIXE, e} + Y_{LD-PIXE, p})]$ is equal to 8.6. Neglecting the proton contribution in LD-EDX (i.e., $Y_{LD-EDX, p}$), we can provide a conservative estimation of the residual x-ray yield due to the electron irradiation in the LD-PIXE experiment [i.e., $Y_{LD-PIXE, e}/(Y_{LD-PIXE, e} + Y_{LD-PIXE, p})$]. We find that <17% and <30% of the x-rays in the LD-PIXE setup are related to surviving electrons instead of protons for the 0.67- and 1.0-MeV electron temperatures, respectively (for detailed calculations, see Materials and Methods). This is coherent with a 10% underestimation of the thickness as found in the previous section.

In Fig. 3 (F and G), we compare the fit of the experimental x-ray Kα peaks and the Monte Carlo simulated spectra for the LD-EDX (with 0.67-MeV electron temperature) and LD-PIXE spectra, respectively. In the LD-EDX simulation, we neglect the proton contribution, while in the LD-PIXE simulation, we neglect the electron one. The counts in each channel are normalized with respect to the total number of characteristic x-rays for Cr and Cu combined. For both spectra, the experimental and simulated peaks are in good agreement. We can also directly compare the simulated and experimental ratios between chromium and copper yields. They are reported as bar plots in Fig. 3 (F and G). Again, we have a reasonable agreement between the experimental data and Monte Carlo simulations. These results give further evidence of the fact that LD-EDX is dominated by the electron contribution to the x-ray production, while in LD-PIXE, the protons are playing the crucial role. Therefore, the proof-of-principle LD-PIXE setup presented in this work is a suitable starting point for the design of a fully optimized system for the removal of the electrons. This aspect is crucial for the development of a reliable LD-PIXE technique.

Last, starting from the experimental and simulated yield ratios, we can provide a post hoc estimation of the electron temperature. By means of analytical calculation (see Materials and Methods), we find that this value is 0.63 ± 0.49 MeV. The result practically coincides with the 0.67-MeV electron temperature that we estimated from laser parameters, while the 1.0-MeV estimation falls within its uncertainty.

We show that a laser-driven particle source can be exploited as a powerful tool to characterize samples of unknown elemental composition. Since this unconventional acceleration scheme provides both high-energy electrons and protons, the experimental setup can be adjusted to perform both LD-EDX and LD-PIXE analyses. We show that LD-EDX can be used to successfully identify the elements with fewer shots compared to LD-PIXE. LD-EDX prospects the possibility, not achievable with traditional EDX, to analyze large artifacts in air and to probe the presence of heavy elements at millimeter depths. Besides, we experimentally demonstrate that LD-PIXE can be used to perform quantitative stratigraphic analysis of a non-homogeneous sample. Thus, LD-EDX and LD-PIXE prove to be complementary techniques for elemental characterization of a sample. Last, on the basis of our results, we suggest that the analyses carried out with a 200-TW laser might be performed also with compact tens of TW class lasers and advanced targetry solutions. Our results represent a remarkable step toward the development of a compact and versatile laser-based radiation source for multiple materials science investigations.

MATERIALS AND METHODS
Chromium film deposition via magnetron sputtering
The Cr film was grown on a pure Cu substrate exploiting a high-power impulse magnetron sputtering deposition system (46) located at Politecnico di Milano. The deposition was performed in DC mode. This technique allows obtaining planar films on large surface areas (several square centimeters). To avoid the delamination of the film due to the strong stresses (47) induced by a long deposition time, we broke the deposition process in several steps. For a complete list of the deposition parameters, see the Supplementary Materials.

CCD energy calibration
CCDs are standard diagnostics for spectroscopy in laser-plasma interaction experiments (26, 48, 49). The Andor IKon-M D0934P-BN CCD camera (1024 × 1024 pixels) energy calibration is performed by exploiting the LD-EDX setup shown in Fig. 1A and a monoelemental sample of pure copper. Figure 4 shows the x-ray spectrum obtained with 16 shots. To perform the energy calibration, we first evaluate the local background distribution around any single-pixel event. By local background, we mean the average intensity related to the eight pixels surrounding a single-pixel event. The distribution is reported in the inset graph of Fig. 4. Its shape is Gaussian, and it is located around 0 to 10 charge-to-signal (cts). Since the x-ray peaks of interest lies around hundreds of cts, we neglect the local background contribution and we directly calibrate the CCD considering the absolute Cu-Kα peak position. The final calibration factor is 8.048 keV/277 cts = 0.029 keV/cts. Using this calibration, we obtain the energies reported in Fig. 2B for all spectra presented in this work. Last, it is worth mentioning that only single-pixel events are considered. The analysis performed on multipixel events reveals that they are extremely rare. Moreover, those events are mainly
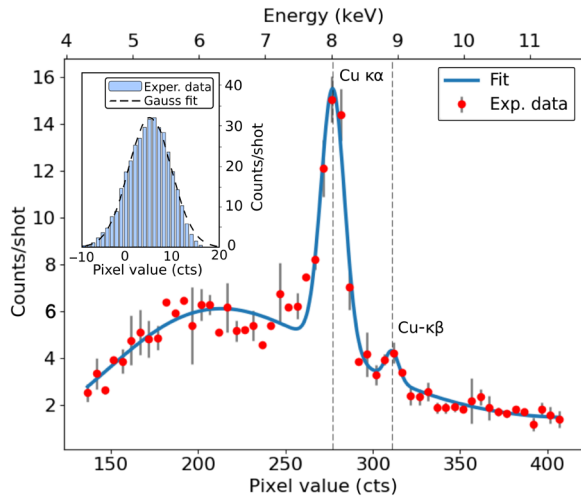
Fig. 4. LD-EDX spectrum for the CCD energy calibration. Copper spectrum obtained with the LD-EDX setup used to calibrate the x-ray CCD. The inset graph is the pixel value distribution of the local background around the single-pixel events.

related to x-rays with energies higher (i.e., $\gtrsim$10 keV) than those of interest for this work.

Additional details about the experimental setup

The Vega-2 laser pulse has 30-fs pulse duration and P-polarization. The energy is 3 J on target, and the intensity is $\sim 2 \times 10^{20}$ W/cm^2. The spot size full width at half maximum is 7.0 μm. The angle of incidence with respect to the target normal is 5°. The thickness of the aluminum target and the protective sheet are 6.0 and 10.0 μm, respectively. As far as the sample is concerned, the chromium film was grown directly on the copper substrate via magnetron sputtering (see previous subsection). The actual composition is 93% chromium and 7% oxygen (expressed as mass fraction). The reported film density equal to 5.3 g/cm^3 has been measured by means of conventional EDX (32) and weight difference between the sample and bare substrate. In the LD-EDX setup, the sample slit is 2.2 μm thick. We place a lead shield to protect the CCD screen from the radiation emitted at the laser-target interaction point. The screen is further protected with 2-μm-thick Mylar and 6-μm-thick aluminum foils.

ToF spectrometer

The ToF spectrometer has been used to characterize the proton spectra. Its location in the experimental setup is shown in Fig. 1A. As ToF diagnostics, we exploited a 1-ns time-resolved pin diode detector. To perform the analysis of the recorded signal, we adopt the approach provided by Milluzzo et al. (28).

Model for LD-PIXE quantitative analysis

For the specific case considered in this work, the x-ray yield Y_{Cr} of Cr due to the incident protons can be expressed with the following equation

$$Y_{Cr} = \varepsilon_{Cr} \frac{W_{Cr}}{M_{Cr}} N_{Av} \times \int_{E_{p,max}}^{E_{p,min}} f_p(E_p) \int_{E_{p,outCr}}^{E_p} \sigma_{Cr}(E) \omega_{Cr} A_{Cr}(E) \frac{dE}{S_{Cr}(E)} dE_p \tag{1}$$

where ε_{Cr} is the CCD efficiency at the Cr x-ray energy and it accounts for both the CCD quantum efficiency (from the instrument documentation) and the attenuation due to the Mylar and aluminum foils, W_{Cr} is the Cr mass concentration in the film, N_{Av} is the Avogadro's number, $E_{p,min}$ and $E_{p,max}$ are the minimum and maximum incident proton energy E_p, $f_p(E_p)$ is the proton spectrum shown in Fig. 1F, $E_{p,outCr}$ is the proton energy at the interface between Cr layer and Cu substrate, σ_{Cr} is the Cr ionization cross section (50, 51), ω_{Cr} is the fluorescence yield (52), and S_{Cr} is the proton stopping power in the Cr layer [from SRIM code (53)]. The proton range inside the sample is linked to the energy with the stopping power through the relation $S(E_p) = -dE/d(\rho t)$. $A_{Cr}(E)$ accounts for the attenuation of the generated x-rays in the Cr layer, and it can be expressed as

$$A_{Cr}(E) = e^{-\mu_{Cr} \int_E^{E_p} \frac{dE'}{S_{Cr}(E)} \frac{\cos\theta}{\cos\varphi}} \tag{2}$$

where μ_{Cr} is the attenuation coefficient of the Cr x-rays in the Cr layer [evaluated with XCOM code (54)], $\theta = 35°$ is the proton incidence angle, and $\varphi = 35°$ is the x-ray emission angle. The equation for the x-ray yield of Cu is

$$Y_{Cu} = \varepsilon_{Cu} \frac{W_{Cu}}{M_{Cu}} N_{Av} \times B \times \int_{E_{p,max}}^{E_{p,min}} f_p(E_p) \int_0^{E_{p,outCu}} \sigma_{Cu}(E) \omega_{Cu} A_{Cu}(E) \frac{dE}{S_{Cu}(E)} dE_p \tag{3}$$

All terms present in the Eq. 3 for Cu have been already described for the Cr case with the exception of B, which accounts for the attenuation of the Cu x-rays is the Cr layer

$$B = e^{-\left(\frac{\mu}{\rho}\right)_{Cr-Cu} \frac{(\rho t)_{Cr}}{\cos\varphi}} \tag{4}$$

where $(\mu/\rho)_{Cr-Cu}$ is the mass attenuation coefficient of the Cu x-rays in the Cr layer. Performing the ratio between Eqs. 1 and 3, we obtain an expression for the x-ray yield ratio Y_{Cr}/Y_{Cu}

$$\frac{Y_{Cr}}{Y_{Cu}} = \frac{\varepsilon_{Cr}}{\varepsilon_{Cu}} \frac{M_{Cu}}{M_{Cr}} \frac{W_{Cr}}{W_{Cu}} \times \frac{\int_{E_{p,max}}^{E_{p,min}} f_p \int_{E_{p,outCr}}^{E_p} \sigma_{Cr} \omega_{Cr} A_{Cr} \frac{dE}{S_{Cr}} dE_p}{B \times \int_{E_{p,max}}^{E_{p,min}} f_p \int_0^{E_{p,outCr}} \sigma_{Cu} \omega_{Cu} A_{Cu} \frac{dE}{S_{Cu}} dE_p} \tag{5}$$

Since both Y_{Cr}/Y_{Cu} and f_p are known from the experiment, Eq. 5 can be solved numerically to find the mass thickness of the Cr layer $(\rho t)_{Cr}$. Because the problem is strongly nonlinear, the solution must be found iteratively. For a more general description of both the analytical model and the iterative algorithm, see the work by Passoni et al. (21).

Error evaluation

To combine the uncertainties on the incident proton spectrum $f_p(E_p)$ and on the yield ratio Y_{Cr}/Y_{Cu}, the measurement error on the layer thickness is evaluated with a Monte Carlo approach. Briefly, we calculate several times the thickness of the sample by means of Eq. 5 and the procedure presented by Passoni et al. (21), changing $f_p(E_p)$ and Y_{Cr}/Y_{Cu} at each evaluation. $f_p(E_p)$ are extracted from the set of recorded spectra. Y_{Cr}/Y_{Cu} values are extracted form a Gaussian distribution. The mean values are 0.91 and 0.37 and the SDs are 0.1687 and 0.0207 for LD-PIXE and LD-EDX, respectively. These values are also reported in Fig. 2B. To obtain the thickness distribution for

the LD-PIXE shown in Fig. 5A, we evaluated the thickness 10^3 times. Consistently with the central limit theorem, the resulting thickness distribution tends to a Gaussian function. We consider its SD as the thickness error. Figure 5B reports the scatter plot of the data obtained with this procedure. This representation is useful to compare the $f_p(E_p)$ and Y_{Cr}/Y_{Cu} contributions to the total uncertainty. Some data obtained in correspondence of the average proton spectrum (red points) and at fixed yield ratio (green points) are superimposed to the heatmap. Since the range covered by red and green points along the vertical direction are comparable, we can conclude that the uncertainties contribute evenly to the total error.

Theoretical evaluations of the electron temperature for Monte Carlo simulations

The electron temperatures of 0.67 and 1.0 MeV exploited in the Monte Carlo simulations are evaluated considering two different approaches. The first value of 0.67 MeV is calculated from the actual laser parameters and the following extended ponderomotive scaling (43)

$$T_e = C_1(a_0, pol, t_{foil}) \cdot 0.511 \cdot \left[\sqrt{1 + \frac{a_0^2}{2}} - 1\right] + C_2(a_0, pol,$$

$$t_{foil}) \cdot 0.511 \cdot \left[\sqrt{\left(1 + f^2 \frac{a_0^2}{2}\right) \sin^3 \theta} - 1\right]\tan\theta \quad (6)$$

where C_1 and C_2 are weighting factors equal to 0.22 and 0.04, respectively, $a_0 = 0.85\sqrt{I\lambda^2/(10^{18}\,\text{W cm}^{-2}\,\mu\text{m}^2)} \cong 9.5$ is the normalized laser amplitude, θ is the laser incidence angle, and $f = 1 + \sqrt{1-\eta}$ is the reflection amplification factor with $\eta \approx 0.1$ as the conversion efficiency of laser energy into hot electrons (which is a reasonable value under our conditions).

The second value of 1.0 MeV is obtained by matching the maximum proton energy measured in our experiment (i.e., ≈ 6.35 MeV) with its estimation obtained through the quasi-static model described by Passoni et al. (44) via the following approximated formula

$$E_{p,max} \approx \left[\ln\frac{n_{h0}}{\tilde{n}} - 1\right] T_e \quad (7)$$

where n_{h0} is the hot electron density and $\tilde{n}$ is a fitting parameter [both computed following, again, the reasoning presented by Passoni et al. (44)].

mFEA simulation

We simulate the 3D static magnetic field created by the structure shown in Fig. 3B with the finite element library Sparselizard (45). A similar 2D example (55) is widely present in the Sparselizard libraries. Please refer to the example for a detailed description of the electrostatic problem and its implementation. Our magnets are characterized by a magnetization equal to 8.0×10^5 A/m. For the permeability of the various regions, we assume $4\pi \times 10^{-7}$ H/m in vacuum and magnet volumes, while in the support volume, we take 10^3 times the value in vacuum. The structure is placed at the center of a cubic box (10-cm face). The simulated mesh is generated with the Gmsh program (56), and it is formed by approximately 2×10^5 nodes. In Fig. 3C, the resulting magnetic field intensity is mapped on three different planes. The magnetic field at the center of the magnet obtained with the simulation coincides with the actual measured value of 0.26 T. Last, we evaluate the magnetic field intensity at the nodes of a $10 \times 10 \times 10$ grid placed between the magnetic plates. In this way, we cover the region of interest where the electrons and ions can travel and, eventually, be deflected. The grid is fed as input in the Geant4 Monte Carlo simulations.

Estimation of the residual x-ray yield due to the electron irradiation in the LD-PIXE experiment

We provide an evaluation of the fraction of x-rays that are still generated by electrons despite the presence of the magnet. The calculations are shown considering the case of 0.67-MeV electron temperature. From the Monte Carlo simulations, the ratio between the x-ray yields due to the electrons in the presence and absence of the magnet is

$$Y_{LD\text{-}PIXE,e}/Y_{LD\text{-}EDX,e} = 0.02 \quad (8)$$

The experimental ratio between the x-ray yields in LD-EDX and LD-PIXE is

$$(Y_{LD\text{-}EDX,e} + Y_{LD\text{-}EDX,p})/(Y_{LD\text{-}PIXE,e} + Y_{LD\text{-}PIXE,p}) = 8.6 \quad (9)$$
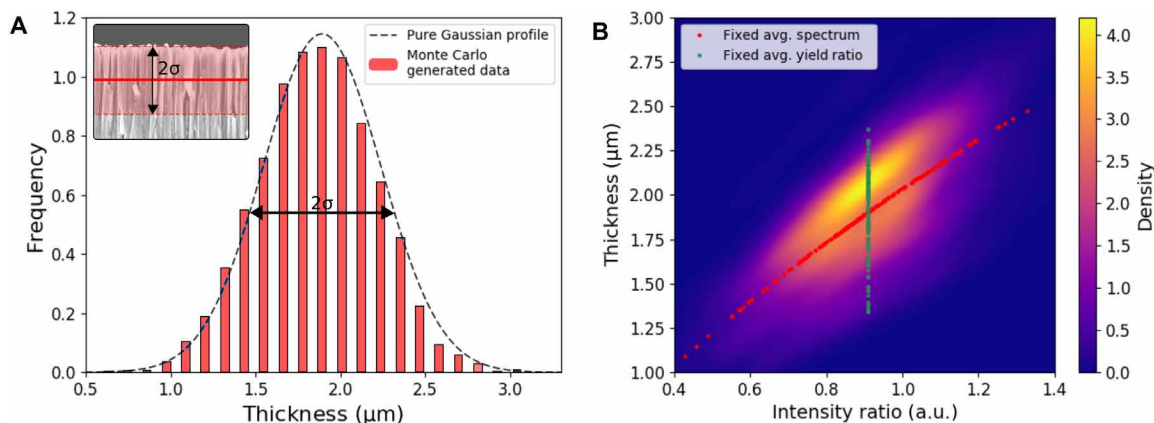

Fig. 5. Uncertainty evaluation for the LD-PIXE measurement. (**A**) Frequency distribution of the thickness resulting from the Monte Carlo simulation for the error calculation. The inset image shows the related uncertainty for the thickness measurement. (**B**) Heatmap scattered data. The extracted intensity ratio is reported on the x axis, while the resulting thickness is on the y axis. The color scale is related to the number of occurrences. The red points are obtained by fixing the proton spectrum as the average one. The green points are obtained by fixing the intensity ratio as the average value.

From Eq. 8, we express $Y_{\text{LD-EDX},e}$ as a function of $Y_{\text{LD-PIXE},e}$ and we perform a substitution in Eq. 9. Rearranging the equation, we obtain the following expression

$$\frac{Y_{\text{LD-PIXE},e}}{Y_{\text{LD-PIXE},e} + Y_{\text{LD-PIXE},p}} = 0.17 \times \left(1 - \frac{0.02 \times Y_{\text{LD-EDX},p}}{Y_{\text{LD-PIXE},e} + Y_{\text{LD-PIXE},p}} \right) \tag{10}$$

The left side of Eq. 10 is the fraction of x-ray yield due to the electron irradiation in the LD-PIXE experiment. The right side of Eq. 10 would be maximized and equal to 0.17 if $Y_{\text{LD-EDX},p}$ is equal to zero. Since $Y_{\text{LD-EDX},p}$ is greater than zero, the expression inside the brackets is definitely lower than 1 and the value 0.17 can be considered an upper threshold for the residual x-ray yield due to the electron irradiation in the LD-PIXE setup. In addition, by neglecting the second term in the brackets (i.e., by assuming $0.02 \times Y_{\text{LD-EDX},p} \approx 0$), Eq. 10 can be further simplified. With a few calculations, it can be found that the ratio between the x-ray yields due to electrons and protons in the LD-PIXE setup $Y_{\text{LD-PIXE},e}/Y_{\text{LD-PIXE},p}$ is less than 0.2 and 0.43 for 0.67- and 1.0-MeV electron temperatures, respectively.

Post hoc estimation of the electron temperature

Exploiting Monte Carlo simulations, the ratio between the copper x-ray yields due to electrons in LD-PIXE and LD-EDX can be fitted as a function of the temperature T_e as

$$Y_{\text{LD-PIXE},e}^{\text{Cu}}/Y_{\text{LD-EDX},e}^{\text{Cu}} = 0.035 \times T_e + 0.0034 \tag{11}$$

The linear fit is shown in Fig. 6. From Monte Carlo simulations, the ratio between the chromium and copper x-ray yields due to electrons in LD-PIXE setup is

$$a = Y_{\text{LD-PIXE},e}^{\text{Cr}}/Y_{\text{LD-PIXE},e}^{\text{Cu}} = 0.65 \tag{12}$$

For reasonable values of T_e, this ratio remains constant. As far as protons are concerned, the ratio is equal to
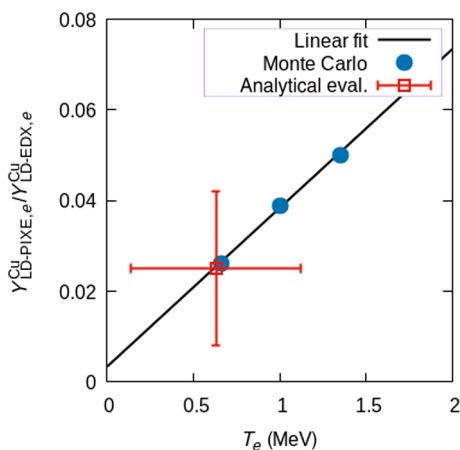
Fig. 6. Linear fit of the electron temperature as a function of the ratio between the copper x-ray yields due to electrons in LD-EDX and LD-PIXE. The blue points are the Monte Carlo simulated data. The black line is the linear fit. The red point is the copper x-ray yield ratio evaluated with the linear fit in correspondence of the electron temperature resulting from the analytical procedure presented in Materials and Methods.

$$b = Y_{\text{LD-PIXE},p}^{\text{Cr}}/Y_{\text{LD-PIXE},p}^{\text{Cu}} = 1.023 \tag{13}$$

From the experimental data, the Cr over Cu x-ray intensity ratio obtained with LD-PIXE is

$$c = (Y_{\text{LD-PIXE},e}^{\text{Cr}} + Y_{\text{LD-PIXE},p}^{\text{Cr}})/(Y_{\text{LD-PIXE},e}^{\text{Cu}} + Y_{\text{LD-PIXE},p}^{\text{Cu}}) = 0.91 \pm 0.169 \tag{14}$$

Last, neglecting the x-ray contribution due to protons in the LD-EDX spectra, we have

$$d = (Y_{\text{LD-PIXE},e}^{\text{Cu}} + Y_{\text{LD-PIXE},p}^{\text{Cu}})/Y_{\text{LD-EDX},e}^{\text{Cu}} = 0.083 \pm 0.011 \tag{15}$$

Combining Eqs. 11 to 15, the electron temperature can be evaluated as

$$T_e = 28.63 \times d \times \frac{b-c}{b-a} - 0.096 = 0.63 \pm 0.49 \text{ MeV} \tag{16}$$

and the corresponding copper x-ray yield ratio is equal to 0.025 ± 0.017. This point is also reported in Fig. 6.

SUPPLEMENTARY MATERIALS

Supplementary material for this article is available at http://advances.sciencemag.org/cgi/content/full/7/3/eabc8660/DC1

REFERENCES AND NOTES

1. H. R. Verma, *Atomic and Nuclear Analytical Methods* (Springer, 2007).
2. D. C. Bell, A. J. Garratt-Reed, *Energy Dispersive X-ray Analysis in the Electron Microscope* (Garland Science, 2003), vol. 49.
3. R. C. Bird, J. S. Williams, *Ion Beams for Materials Analysis* (Elsevier, 1990).
4. A. G. Karydas, C. Streeck, I. Bogdanovic Radovic, C. Kaufmann, T. Rissom, B. Beckhoff, M. Jaksic, N. P. Barradas, Ion beam analysis of Cu(In,Ga)Se₂ thin film solar cells. *Appl. Surf. Sci.* **356**, 631–638 (2015).
5. D. Nam, A. S. Opanasyuk, P. V. Koval, A. G. Ponomarev, A. R. Jeong, G. Y. Kim, W. Jo, H. Cheong, Composition variations in Cu₂ZnSnSe₄ thin films analyzed by x-ray diffraction, energy dispersive x-ray spectroscopy, particle induced x-ray emission, photoluminescence, and Raman spectroscopy. *Thin Solid Films* **562**, 109–113 (2014).
6. C. Q. Orsini, L. C. Boueres, A PIXE system for air pollution studies in South America. *Nucl. Instrum. Methods.* **142**, 27–32 (1977).
7. E. Wyroba, S. Suski, K. Miller, R. Bartosiewicz, Biomedical and agricultural applications of energy dispersive x-ray spectroscopy in electron microscopy. *Cell. Mol. Biol. Lett.* **20**, 488–509 (2015).
8. Ž. Šmit, M. Uršič, P. Pelicon, T. Trček-Pečak, B. Šeme, A. Smrekar, I. Langus, I. Nemec, K. Kavkler, Concentration profiles in paint layers studied by differential PIXE. *Nucl. Instrum. Methods Phys. Res. B* **266**, 2047–2059 (2008).
9. A. G. Shen, X. H. Wang, W. Xie, J. Shen, H. Y. Li, Z. A. Liu, M. H. Jing, Pigment identification of colored drawings from Wuying Hall of the Imperial Palace by micro-Raman spectroscopy and energy dispersive x-ray spectroscopy. *J. Raman Spectrosc.* **37**, 230–234 (2006).
10. A. Macchi, M. Borghesi, M. Passoni, Ion acceleration by superintense laser-plasma interaction. *Rev. Mod. Phys.* **85**, 751–793 (2013).
11. V. Malka, J. Faure, Y. A. Gauduel, E. Lefebvre, A. Rousse, K. T. Phuoc, Principles and applications of compact laser-plasma accelerators. *Nat. Phys.* **4**, 447–453 (2008).
12. H. Daido, M. Nishiuchi, A. S. Pirozhkov, Review of laser-driven ion sources and their applications. *Rep. Prog. Phys.* **75**, 056401 (2012).
13. F. P. Boody, R. Höpfl, H. Hora, J. C. Kelly, Laser-driven ion source for reduced-cost implantation of metal ions for strong reduction of dry friction and increased durability. *Laser Part. Beams.* **14**, 443–448 (1996).
14. M. Nishiuchi, H. Daido, A. Sagisaka, K. Ogura, S. Orimo, M. Kado, A. Yogo, M. Mori, Y. Hayashi, S. Bulanov, A. Fukumi, Z. Li, A. Noda, S. Nakamura, Repetitive highly collimated intense proton beam with sub-MeV energy range driven by a compact few terawatt femtosecond laser. *Appl. Phys. B* **87**, 615–621 (2007).
15. L. J. Perkins, B. G. Logan, M. D. Rosen, M. D. Perry, T. Diaz de La Rubia, N. M. Ghoniem, T. Ditmire, P. T. Springer, S. C. Wilks, The Investigation of high intensity laser driven micro neutron sources for fusion materials research at high fluence. *Nucl. Fusion.* **40**, 1–19 (2000).

16. F. SourceLab, Orsay, SL-KAIO: Plug & play ion generator, https://perma.cc/4G84-LE2U.

17. Thales, TeraWatt Systems, https://perma.cc/9FNG-JV7X.

18. TT-MOBILE, Integrated mobile laser system for filamentation in air, https://perma.cc/9X8D-N2DD.

19. Amplitude Laser, Pulsar TW, https://perma.cc/69M9-WDJA.

20. M. Passoni, F. M. Arioli, L. Cialfi, D. Dellasega, L. Fedeli, A. Formenti, A. C. Giovannelli, A. Maffini, F. Mirani, A. Pazzaglia, A. Tentori, D. Vavassori, M. Zavelani-Rossi, V. Russo, Advanced laser-driven ion sources and their applications in materials and nuclear science. *Plasma Phys. Control. Fusion.* **62**, 14022 (2019).

21. M. Passoni, L. Fedeli, F. Mirani, Superintense laser-driven ion beam analysis. *Sci. Rep.* **9**, 9202 (2019).

22. M. Barberio, S. Veltri, M. Sciscià, P. Antici, Laser-accelerated proton beams as diagnostics for cultural heritage. *Sci. Rep.* **7**, 40415 (2017).

23. M. Barberio, P. Antici, Laser-PIXE using laser-accelerated proton beams. *Sci. Rep.* **9**, 6855 (2019).

24. A. Flacco, F. Sylla, M. Veltcheva, M. Carrié, R. Nuter, E. Lefebvre, D. Batani, V. Malka, Dependence on pulse duration and foil thickness in high-contrast-laser proton acceleration. *Phys. Rev. E* **81**, 036405 (2010).

25. L. Volpe, R. Fedosejevs, G. Gatti, J. A. Pérez-Hernández, C. Méndez, J. Apiñaniz, X. Vaisseau, C. Salgado, M. Huault, S. Malko, G. Zeraouli, V. Ospina, A. Longman, D. De Luis, K. Li, O. Varela, E. García, I. Hernández, J. D. Pisonero, J. G. Ajates, J. M. Alvarez, C. García, M. Rico, D. Arana, J. Hernández-Toro, L. Roso, Generation of high energy laser-driven electron and proton sources with the 200 TW system VEGA 2 at the Centro de Laseres Pulsados. *High Power Laser Sci. Eng.* **7**, e25 (2019).

26. C. Stoeckl, W. Theobald, T. Sangster, M. Key, P. K. Patel, B. Zhang, R. Clarke, S. Karsch, P. Norreys, Operation of a single-photon-counting x-ray charge-coupled device camera spectrometer in a petawatt environment. *Rev. Sci. Instrum.* **75**, 3705–3707 (2004).

27. J. Baumann, R. Gnewkow, S. Staeck, V. Szwedowski-Rammert, C. Schlesiger, I. Mantouvalou, B. Kanngießer, Photon event evaluation for conventional pixelated detectors in energy-dispersive x-ray applications. *J. Anal. At. Spectrom* **33**, 2043–2052 (2018).

28. G. Milluzzo, V. Scuderi, A. Alejo, A. G. Amico, N. Booth, M. Borghesi, G. A. P. Cirrone, G. Cuttone, D. Doria, J. Green, S. Kar, G. Korn, G. Larosa, R. Leanza, D. Margarone, P. Martin, P. McKenna, G. Petringa, J. Pipek, L. Romagnani, F. Romano, A. Russo, F. Schillaci, A new energy spectrum reconstruction method for time-of-flight diagnostics of high-energy laser-driven protons. *Rev. Sci. Instrum.* **90**, 083303 (2019).

29. J. Prokůpek, D. Margarone, D. Kramer, T. Mocek, J. Limpouch, I. J. Kim, T. M. Jeong, K. H. Nam, G. Bertuccio, D. Puglisi, G. Korn, Experimental test of TOF diagnostics for PW class lasers, Proceedings SPIE 8779, Laser Acceleration of Electrons, Protons, and Ions II; and Medical Applications of Laser-Generated Beams of Particles II; and Harnessing Relativistic Plasma Waves III (2013), vol. 87790W.

30. P. R. Bevington, D. K. Robinson, *Data Reduction and Error Analysis for the Physical Sciences* (McGraw-Hill, 1969).

31. R. Van Grieken, A. Markowicz, *Handbook of X-ray Spectrometry* (CRC Press, 2001).

32. A. Pazzaglia, A. Maffini, D. Dellasega, A. Lamperti, M. Passoni, Reference-free evaluation of thin films mass thickness and composition through energy dispersive X-ray spectroscopy. *Mater Charact.* **153**, 92–102 (2019).

33. M. G. Cox, B. R. L. Siebert, The use of a Monte Carlo method for evaluating uncertainty and expanded uncertainty. *Metrologia* **43**, S178–S188 (2006).

34. X. Llovet, C. J. Powell, F. Salvat, A. Jablonski, Cross sections for inner-shell ionization by electron impact. *J. Phys. Chem. Ref. Data.* **43**, 013102 (2014).

35. D. Neely, P. Foster, A. Robinson, F. Lindau, O. Lundh, A. Persson, C.-G. Wahlström, P. McKenna, Enhanced proton beams from ultrathin targets driven by high contrast laser pulses. *Appl. Phys. Lett.* **89**, 021502 (2006).

36. T. Ceccotti, A. Lévy, H. Popescu, F. Réau, P. D'Oliveira, P. Monot, J. P. Geindre, E. Lefebvre, P. Martin, Proton acceleration with high-intensity ultrahigh-contrast laser pulses. *Phys. Rev. Lett.* **99**, 185002 (2007).

37. N. Grassi, A. Migliori, P. A. Mandò, H. Calvo del Castillo, Differential PIXE measurements for the stratigraphic analysis of the painting *Madonna dei fusi* by Leonardo da Vinci. *X-Ray Spectrom.* **34**, 306–309 (2005).

38. M. Gauthier, C. B. Curry, S. Göde, F. E. Brack, J. B. Kim, M. J. MacDonald, J. Metzkes, L. Obst, M. Rehwald, C. Rödel, H. P. Schlenvoigt, W. Schumaker, U. Schramm, K. Zeil, S. H. Glenzer, High repetition rate, multi-MeV proton source from cryogenic hydrogen jets. *Appl. Phys. Lett.* **111**, 114102 (2017).

39. I. Prencipe, I. Prencipe, A. Sgattoni, D. Dellasega, L. Fedeli, L. Cialfi, I. W. Choi, I. Kim, K. Janulewicz, K. Kakolee, H. Lee, J. Sung, S. Lee, C. H. Nam, M. Passoni, Development of foam-based layered targets for laser-driven ion beam production. *Plasma Phys. Control. Fusion.* **58**, 034019 (2016).

40. A. Pazzaglia, L. Fedeli, A. Formenti, A. Maffini, M. Passoni, A theoretical model of laser-driven ion acceleration from near-critical double-layer targets. *Commun. Phys.* **3**, 133 (2020).

41. M. Passoni, A. Sgattoni, I. Prencipe, L. Fedeli, D. Dellasega, L. Cialfi, I. W. Choi, I. J. Kim, K. . A. Janulewicz, H. W. Lee, J. H. Sung, S. K. Lee, C. H. Nam, Toward high-energy

laser-driven ion beams: Nanostructured double-layer targets. *Phys. Rev. Accel. Beams.* **19**, 061301 (2016).

42. J. Allison, K. Amako, J. Apostolakis, P. Arce, M. Asai, T. Aso, E. Bagli, A. Bagulya, S. Banerjee, G. Barrand, B. R. Beck, A. G. Bogdanov, D. Brandt, J. M. C. Brown, H. Burkhardt, P. Canal, D. Cano-Ott, S. Chauvie, K. Cho, G. A. P. Cirrone, G. Cooperman, M. A. Cortés-Giraldo, G. Cosmo, G. Cuttone, G. Depaola, L. Desorgher, X. Dong, A. Dotti, V. D. Elvira, G. Folger, Z. Francis, A. Galoyan, L. Garnier, M. Gayer, K. L. Genser, V. M. Grichine, S. Guatelli, P. Guèye, P. Gumplinger, A. S. Howard, I. Hřivnáčová, S. Hwang, S. Incerti, A. Ivanchenko, V. N. Ivanchenko, F. W. Jones, S. Y. Jun, P. Kaitaniemi, N. Karakatsanis, M. Karamitros, M. Kelsey, A. Kimura, T. Koi, H. Kurashige, A. Lechner, S. B. Lee, F. Longo, M. Maire, D. Mancusi, A. Mantero, E. Mendoza, B. Morgan, K. Murakami, T. Nikitina, L. Pandola, P. Paprocki, J. Perl, I. Petrović, M. G. Pia, W. Pokorski, J. M. Quesada, M. Raine, M. A. Reis, A. Ribon, A. R. Fira, F. Romano, G. Russo, G. Santin, T. Sasaki, D. Sawkey, J. I. Shin, I. I. Strakovsky, A. Taborda, S. Tanaka, B. Tomé, T. Toshito, H. N. Tran, P. R. Truscott, L. Urban, V. Uzhinsky, J. M. Verbeke, M. Verderi, B. L. Wendt, H. Wenzel, D. H. Wright, D. M. Wright, T. Yamashita, J. Yarba, H. Yoshida, Recent developments in GEANT4. *Nucl. Instrum. Methods Phys. Res. A* **835**, 186–225 (2016).

43. L. Cialfi, L. Fedeli, M. Passoni, Electron heating in subpicosecond laser interaction with overdense and near-critical plasmas. *Phys. Rev. E.* **94**, 053201 (2016).

44. M. Passoni, C. Perego, A. Sgattoni, D. Batani, Advances in target normal sheath acceleration theory. *Phys. Plasmas.* **20**, 060701 (2013).

45. A. Halbach, Sparselizard—The user friendly finite element C++ library (2017); http://hdl.handle.net/2268/216780.

46. P. J. Kelly, R. D. Arnell, Magnetron sputtering: A review of recent developments and applications. *Vacuum* **56**, 159–172 (2000).

47. G. Abadias, G. Abadias, E. Chason, J. Keckes, M. Sebastiani, G. Thompson, E. Barthel, G. Doll, C. E. Murray, C. H. Stoessel, L. Martinů, Review Article: Stress in thin films and coatings: Current status, challenges, and prospects. *J. Vac. Sci. Technol. A Vacuum, Surfaces, Film.* **36**, 020801 (2018).

48. W. Hong, X.-L. Wen, X. Wei, L. Bu, B. Zhu, Y.-C. Wu, K.-G. Dong, C.-Y. Jiao, B. Wu, Y.-L. He, F.-Q. Zhang, W.-M. Zhou, Y.-Q. Gu, Detailed calibration of the PI-LCX:1300 high performance single photon counting hard x-ray CCD camera. *Chin. Phys. B.* **26**, 025204 (2017).

49. S. A. Pikuz, O. V. Chefonov, S. V. Gasilov, P. S. Komarov, A. V. Ovchinnikov, I. Y. Skobelev, S. Y. Ashitkov, M. V. Agranat, A. Zigler, A. Y. Faenov, Micro-radiography with laser plasma x-ray source operating in air atmosphere. *Laser Part. Beams.* **28**, 393–397 (2010).

50. W. Brandt, G. Lapicki, Energy-loss effect in inner-shell Coulomb ionization by heavy charged particles. *Phys. Rev. A* **23**, 1717–1729 (1981).

51. W. Brandt, G. Lapicki, *L*-shell Coulomb ionization by heavy charged particles. *Phys. Rev. A* **20**, 465–480 (1979).

52. A. Kahoul, A. Abassi, B. Deghfel, M. Nekkab, K-shell fluorescence yields for elements with 6≤Z≤99. *Radiat. Phys. Chem.* **80**, 369–377 (2011).

53. J. F. Ziegler, M. D. Ziegler, J. P. Biersack, SRIM—The stopping and range of ions in matter (2010). *Nucl. Instrum. Methods Phys. Res. B* **264**, 1818–1823 (2010).

54. M. J. Berger, J.H. Hubbell, S.M. Seltzer, J. Chang, J.S. Coursey, R. Sukumar, D.S. Zucker, K. Olsen, XCOM: Photon cross sections database (2010); https://dx.doi.org/10.18434/T48G6X.

55. A. Halbach, PERMANENT MAGNETS, MAGNETIC FORCE, https://github.com/halbux/sparselizard/blob/master/examples/magnetostatics-scalar-potential-2d/main.cpp.

56. C. Geuzaine, J.-F. Remacle, Gmsh: A 3-D finite element mesh generator with built-in pre- and post-processing facilities. *Int. J. Numer. Methods Eng.* **79**, 1309–1331 (2009).

Citation: F. Mirani, A. Maffini, F. Casamichiela, A. Pazzaglia, A. Formenti, D. Dellasega, V. Russo, D. Vavassori, D. Bortot, M. Huault, G. Zeraouli, V. Ospina, S. Malko, J. I. Apiñaniz, J. A. Pérez-Hernández, D. De Luis, G. Gatti, L. Volpe, A. Pola, M. Passoni, Integrated quantitative PIXE analysis and EDX spectroscopy using a laser-driven particle source. *Sci. Adv.* **7**, eabc8660 (2021).

Science Advances

Integrated quantitative PIXE analysis and EDX spectroscopy using a laser-driven particle source

F. Mirani, A. Maffini, F. Casamichiela, A. Pazzaglia, A. Formenti, D. Dellasega, V. Russo, D. Vavassori, D. Bortot, M. Huault, G. Zeraouli, V. Ospina, S. Malko, J. I. Apiñaniz, J. Á. Pérez-Hernández, D. De Luis, G. Gatti, L. Volpe, A. Pola and M. Passoni

ARTICLE TOOLS	http://advances.sciencemag.org/content/7/3/eabc8660
SUPPLEMENTARY MATERIALS	http://advances.sciencemag.org/content/suppl/2021/01/11/7.3.eabc8660.DC1
REFERENCES	This article cites 43 articles, 0 of which you can access for free http://advances.sciencemag.org/content/7/3/eabc8660#BIBL
PERMISSIONS	http://www.sciencemag.org/help/reprints-and-permissions

Use of this article is subject to the Terms of Service